(article starts on next page)

Overview of the FTU results

G. Pucella[1,*], E. Alessi[2], S. Almaviva[1], B. Angelini[1], M.L. Apicella[1],
G. Apruzzese[1], M. Aquilini[1], G. Artaserse[1], B. Baiocchi[2], M. Baruzzo[1],
F. Belli[1], W. Bin[2], F. Bombarda[1], L. Boncagni[1], S. Briguglio[1], A. Bruschi[2],
P. Buratti[1], G. Calabrò[3], M. Cappelli[1], A. Cardinali[1], N. Carlevaro[1],
D. Carnevale[4], L. Carraro[5], C. Castaldo[1], F. Causa[2], R. Cavazzana[5],
S. Ceccuzzi[1], P. Cefali[1], C. Centioli[1], R. Cesario[1], S. Cesaroni[4],
C. Cianfarani[1], M. Ciotti[1], G. Claps[1], F. Cordella[1], F. Crisanti[1], Y. Damizia[6],
O. D'Arcangelo[1], M. De Angeli[2], E. Di Ferdinando[1], S. Di Giovenale[1],
C. Di Troia[1], A. Dodaro[1], B. Esposito[1], M. Falessi[1], F. Fanale[2], D. Farina[2],
L. Figini[2], G. Fogaccia[1], D. Frigione[1], V. Fusco[1], L. Gabellieri[1],
G. Gallerano[1], S. Garavaglia[2], G. Ghillardi[1], G. Giacomi[1],
E. Giovannozzi[1], G. Gittini[2], G. Granucci[2], G. Grosso[2], L.A. Grosso[1],
M. Iafrati[1], L. Laguardia[2], E. Lazzaro[2], D. Liuzza[1], M. Lontano[2],
G. Maddaluno[1], S. Magagnino[1], M. Marinucci[1], D. Marocco[1], G. Mazzitelli[1],
C. Mazzotta[1], C. Meineri[1], V. Mellera[2], M. Mezzacappa[1], A. Milovanov[1],
D. Minelli[2], F.C. Mirizzi[7], G. Montani[1], A. Moro[2], F. Napoli[1], S. Nowak[2],
F.P. Orsitto[1], D. Pacella[1], F. Pallotta[2], S. Palomba[4], L. Panaccione[7],
A. Pensa[1], V. Pericoli-Ridolfini[7], P. Petrolini[1], V. Piergotti[1], C. Piron[1],
A. Pizzuto[1], S. Podda[1], M.E. Puiatti[5], G. Ramogida[1], B. Raspante[1],
G. Ravera[1], D. Ricci[2], N. Rispoli[2], G. Rocchi[1], A. Romano[1], G. Rubino[3],
S. Rueca[1], M. Scisciò[1], L. Senni[1], A. Sibio[1], A. Simonetto[2], C. Sozzi[2],
U. Tartari[2], A. Taschin[1], B. Tilia[1], G. Trentuno[1], A.A. Tuccillo[1], O. Tudisco[1],
R. Tulli[1], M. Valisa[5], M. Vellucci[1], B. Viola[1], E. Vitale[1], G. Vlad[1], D. Zannetti[1],
B. Zaniol[5], M. Zerbini[1], F. Zonca[1], V.K. Zotta[8], M. Angelone[1],
C. Barcellona[9], L. Calacci[4], L. Caneve[1], F. Colao[1], B. Coppi[10], S. Galeani[4],
C. Galperti[11], P. Gasior[12], W. Gromelski[12], M. Hoppe[13], M. Kubkowska[12],
V. Lazic[1], M. Lehnen[14], M. Marinelli[4], F. Martinelli[4], E. Milani[4], P. Mosetti[1],
P. Muscente[15], E. Nardon[16], M. Passeri[4], A. Reale[1], M. Sassano[4], A. Selce[1],
C. Verona[4] and G. Verona-Rinati[4]

[1] ENEA, Fusion and Nuclear Safety Department, C.R. Frascati, Via E. Fermi 45, 00044 Frascati, Italy
[2] Institute for Plasma Science and Technology, National Research Council of Italy, Via R. Cozzi 53, 20125 Milano, Italy
[3] Università della Tuscia, Centre for Research and Dissemination of Renewable Energy, 01028 Orte, Italy
[4] Università di Roma Tor Vergata, Facoltà di Ingegneria, Via del Politecnico 1, 00133 Roma, Italy
[5] Consorzio RFX (CNR, ENEA, INFN, Univ. Padova, Acciaierie Venete Spa), Corso Stati Uniti 4, 35127 Padova, Italy
[6] Università di Roma La Sapienza, Facoltà di Fisica, Piazzale Aldo Moro 5, 00185 Roma, Italy
[7] Consorzio CREATE, Università di Napoli Federico II, Via Claudio 21, 80125 Napoli, Italy
[8] Università di Roma La Sapienza, Facoltà di Ingegneria, Piazzale Aldo Moro 5, 00185 Roma, Italy
[9] Università di Catania, Dip. di Ing. Elettrica, Elettronica e Informatica, 95125 Catania, Italy
[10] Massachusetts Institute of Technology, MA 02139 Cambridge, United States of America
[11] Swiss Plasma Centre-École polytechnique fédérale de Lausanne, Lausanne, Switzerland
[12] IPPLM Institute of Plasma Physics and Laser Microfusion, Hery Street 23, 01-497 Warsaw, Poland

* Author to whom any correspondence should be addressed.

[13] Chalmers University of Technology, Department of Physics, SE-41296 Gothenburg, Sweden
[14] ITER Organization, Route de Vinon sur Verdon, 13115 St Paul Lez Durance, France
[15] Università di Padova, Centro di Ateneo 'Centro Ricerche Fusione' c/o Consorzio RFX, Padova, Italy
[16] CEA, IRFM, F-13108, Saint Paul-lez-Durance, France

E-mail: gianluca.pucella@enea.it

Abstract

Since the 2018 IAEA FEC Conference, FTU operations have been devoted to several experiments covering a large range of topics, from the investigation of the behaviour of a liquid tin limiter to the runaway electrons mitigation and control and to the stabilization of tearing modes by electron cyclotron heating and by pellet injection. Other experiments have involved the spectroscopy of heavy metal ions, the electron density peaking in helium doped plasmas, the electron cyclotron assisted start-up and the electron temperature measurements in high temperature plasmas. The effectiveness of the laser induced breakdown spectroscopy system has been demonstrated and the new capabilities of the runaway electron imaging spectrometry system for in-flight runaways studies have been explored. Finally, a high resolution saddle coil array for MHD analysis and UV and SXR diamond detectors have been successfully tested on different plasma scenarios.

Keywords: overview, FTU, FEC

(Some figures may appear in colour only in the online journal)

1. Introduction

FTU is a compact high magnetic field machine (toroidal magnetic field B_T up to 8 T, plasma current I_p up to 1.6 MA) with a circular poloidal cross section (major radius $R_0 = 0.935$ m, minor radius $a = 0.30$ m) and metallic first wall [1]. The stainless steel vacuum chamber has a thickness of 2 mm and is covered internally by a toroidal limiter made of 2 cm thick molybdenum tiles, and an outer molybdenum poloidal limiter is also present. In order to reduce the oxygen content, FTU walls are conditioned with boron coating at the beginning of any experimental campaign. Since the 2018 IAEA Fusion Energy Conference in Gandhinagar, FTU operations were largely devoted to experiments on liquid metal limiters, runaway electrons REs and MHD stability and control. Other experiments have involved the spectroscopy of heavy metal ions, the helium doped plasmas and the electron cyclotron assisted start-up. New diagnostics have been successfully installed and tested, and new capabilities of previously installed diagnostics have been explored.

2. Liquid metal limiters

FTU can be considered a pioneer and leader device in liquid metal investigation as a plasma facing material and it was the first tokamak in the world that has performed experiments using a liquid lithium limiter and a liquid tin limiter [2]. The liquid metal limiters were inserted from a vertical port at the bottom side of the machine, and then the radial position could be moved shot by shot from the radius of the vacuum chamber wall ($r = 33.5$ cm) up to $r = 27.5$ cm, namely some centimetres closer to the plasma centre than the titanium–zirconium–molybdenum (TZM) alloy toroidal main FTU limiter ($r = 30.0$ cm). After plasma exposure, the limiters could be extracted in a separate volume where an optical window permits a visual inspection of the surface. All of the experiments with liquid metals on FTU have been performed following the static approach: the liquid metal has been kept confined using a capillary porous system (CPS). The porous structure confines the liquid metal and hinders the potential MHD melt motion owing to electromagnetic loads that arise during transients events [3, 4]. The impact of the two elements (Li and Sn) on the plasma performances has been well assessed. The allowed temperature windows extensively discussed in literature [5] have been investigated and validated for the first time in a medium size tokamak. The most relevant difference between lithium and tin is the atomic number (i.e. $Z = 3$ for lithium and $Z = 50$ for tin), which is strongly related with radiated power. Lithium mainly emits in the scrape-off layer, while tin also emits in the plasma core. This means that lithium density in the order of a few percent of the electron density can be withstood by the plasma with no performance degradation, while for tin the maximum allowed contamination is in the order of 10^{-4} of the electron density. Several experiments on FTU suggested that if the liquid tin surface temperature was below the evaporation onset (namely below
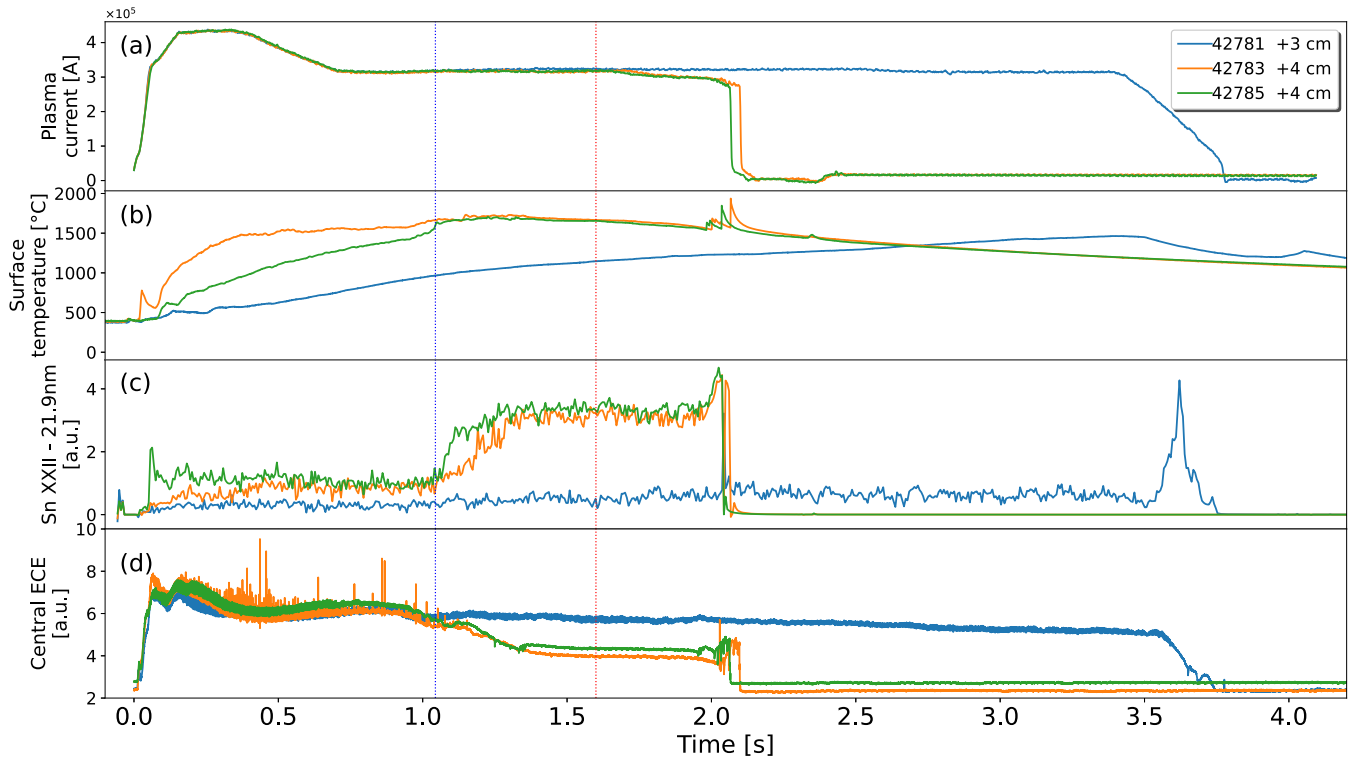
Figure 1. Liquid metal limiters. From top to bottom: (*a*) plasma current, (*b*) limiter surface temperature, (*c*) Sn XXII (21.9 nm) line integral, (*d*) central ECE. The strong increase in the plasma impurity content (see the tin line integral in (*c*)) is observed when the surface temperature exceeds the tolerable operative range (shots 42783 and 42785). The ECE drop and subsequent loss of the sawtooth activity lead to the plasma disruption.

1500 °C), the plasma performances appeared unaffected (heat loads in excess of 18 MW m^{-2} were withstood by the liquid tin limiter for approximately 1 s).

Recently, soft x-ray and electron cyclotron emissions (ECE) have been analysed to extend the core plasma characterization on MHD internal activity. In figure 1, a set of three shots is shown. In shot 42781 (blue), the limiter was inserted 3 cm inside the vacuum chamber, whilst in shots 42783 (orange) and 42785 (green) the limiter was inserted 4 cm in order to increase the interaction with the plasma and consequently the heat load on the liquid tin surface. In these two shots, it acted as the main limiter and the heat flux was enough to bring the surface temperature to the upper limit value. When the surface temperature exceeds 1500 °C (*b*), a strong increase of the tin line integral occurs (*c*). Consequently, the central ECE drops (*d*) and the sawtooth activity is lost due to tin accumulation in the core region leading to a plasma disruption. The experience gained during the FTU experiments [6] is the basis of the design choices of the liquid metal divertor (LMD) within the context of the EUROfusion FP8 WP-DTT1-LMD (deliverable D8.10). From such experience, an LMD concept design, CPS-based, has been purposed to DEMO. Tin has been preferred as the plasma facing material. The proposed LMD would operate in the low evaporative regime, with matching heat exhausting capabilities to those of the baseline DEMO-like divertor [7].

3. Runaway electrons studies

Runaway electrons (REs) beam generated during disruptions are considered one of the main concerns for large tokamaks such as ITER. Different strategies are currently investigated, mainly hinging on RE suppression before the RE beam formation, i.e. injecting high-Z particles via shattered pellet injections and/or massive gas injection to dissipate RE energy by collisions [8]. However, this approach shows alarming limitations due to assimilation rate and efficiency, also due to the necessity to cope with thermal and electromechanical constraints that impose a narrow time window on such types of mitigation. Alternative or parallel strategies involve active control via dedicated control algorithm [9], resonant magnetic perturbation [10], and triggering kink instabilities on fully formed RE beam to widen the energy deposition area [11], but further studies are still needed in order to define a reliable and safe strategy for ITER.

Continuing our investigation on this topic, we studied the effects of D_2 pellet injections on RE quiescent discharges. We have found that single or multiple pellet injections on 0.5 MA current discharges lead to complete suppression of RE seeding by triggering bursts of MHD activity, which expel REs (see figure 2). The high repeatability of such results, which mimic the natural REs expulsion that sometimes are observed in RE quiescent discharges by burst MHD activity, could
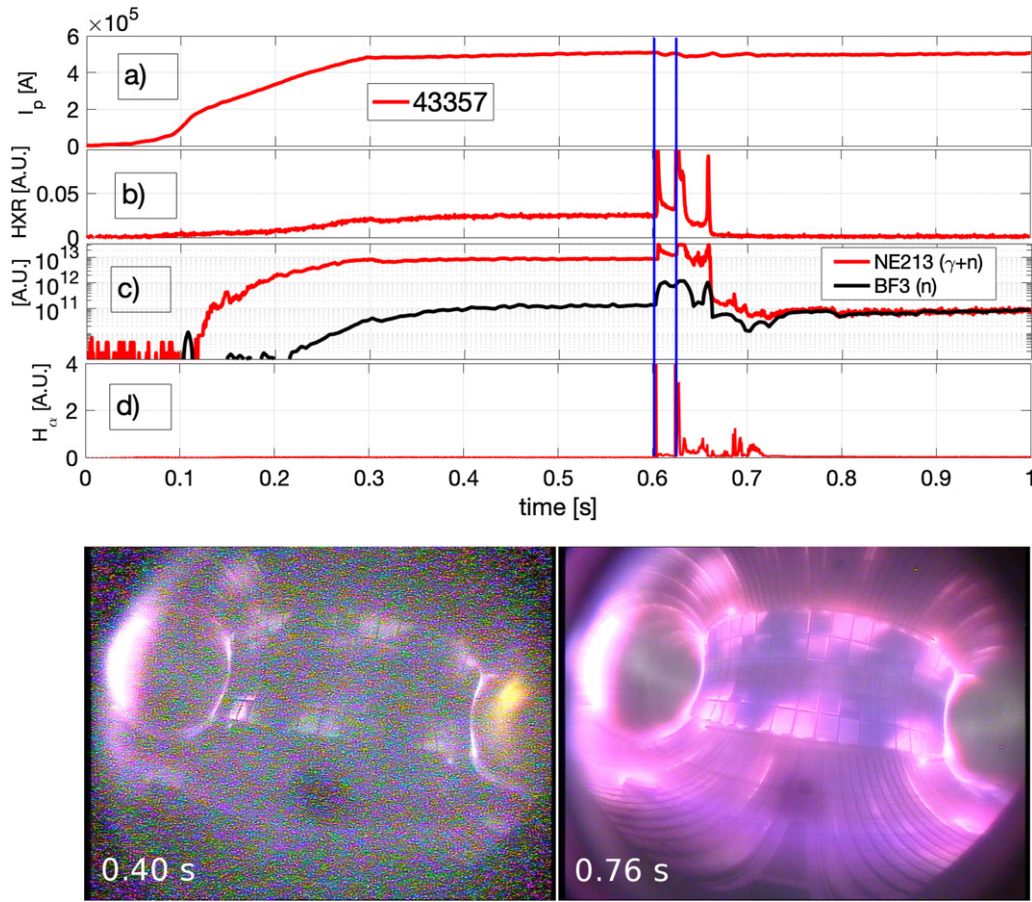
Figure 2. Runaway electrons studies. D_2 pellet injections at times (vertical blue lines in top panels) 0.60 s (1×10^{20} atoms) and 0.62 s (2×10^{20} atoms) on RE quiescent discharge 43357: almost unperturbed plasma current (*a*), complete loss of REs as shown by collapse of signal NE213 on signal BF3 (*c*) and corresponding decrease to zero of hard x-ray (HXR) signal (*b*), H_α signal (*d*). (Bottom left) Visible synchrotron emission of quiescent REs and healed discharge after pellets (bottom right).

suggest an RE mitigation pre-emptive strategy on ITER. In the case of 0.35 MA RE quiescent discharges, different effects have been found with pellet injections. In most cases, we observed an exponential growth of RE population up to the saturation of gamma-ray detector (liquid scintillator NE213), approximately 60 ms after the pellet injection. To explain such exponential REs growth, avalanche generation has to be accounted for, since primary generation is not compatible with such fast growth. In a few other cases, pellet injection leads to a disruption generating an RE beam.

Further ongoing studies focus on the possibility of reducing the RE beam energy during its formation providing a large electron population at current quench (CQ). Indeed, we found cases in which pellets launched closely to CQ seem to lead to lower energy and higher current RE beams. A possible explanation is that the increased number of free electrons, combined with the high-Z particles flushing-out property of D_2 pellet, allows distributed absorption of the electrical field at CQ limiting the maximal energy of REs, as well as improving the RE beam controllability due to the reduced current drop, which is very important from a control point of view and permits other dissipation strategies requiring RE beam stabilization. On the post-disruption RE beam, for the first time at FTU, a density increase has been observed after D_2

pellet injection as well as laser blow-off (LBO) ionization (and drag effects), proving increased background plasma temperature: fan-like instabilities (see section 4) seem to play an important role transferring energy to background plasma. Modulated electron cyclotron resonance heating (ECRH) on post-disruption RE beam induced interesting synchronization of fan-like and MHD driven instabilities and new interesting observations of REs interaction with large magnetic island have been performed [12].

4. Measurements of plasma waves emitted by runaway electrons

Interactions between REs and plasma waves can enlarge RE pitch-angle scattering, leading to larger synchrotron losses, which in turn enhance the critical electric field for avalanche multiplication and reduce the maximum energy of RE. Plasma waves emission by RE was studied both theoretically [13] and experimentally [14], with the aim of developing advanced RE mitigation methods.

The emission of radio waves by RE has been measured on FTU under different plasma regimes, including low-density hot plasmas, pellet-fueled plasmas and post-disruption RE beams. The explored range of the ratio between electron
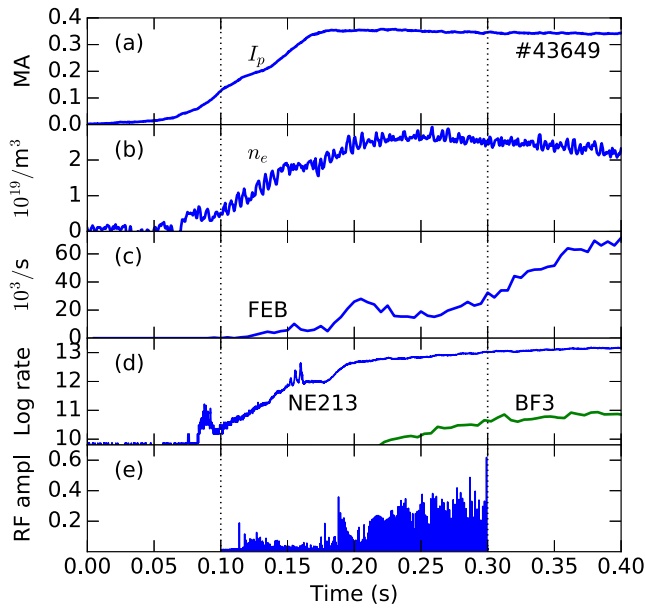
Figure 3. Measurements of plasma waves emitted by runaway electrons. FTU pulse 43649 at 5.3 T. (*a*) Plasma current. (*b*) Line-averaged density from the central chord of a CO_2 laser interferometer. (*c*) HXR count rate from an equatorial channel of the fast electron bremsstrahlung camera. (*d*) Log_{10} of HXR and neutron count rate from a Nuclear Enterprises liquid organic scintillator (NE213) sensitive to both HXR and neutrons; the neutron contribution from cross-calibrated boron trifluoride (BF_3) neutron detectors is shown by the lower line. (*e*) Radiofrequency emission amplitude from moving RMS, normalized to digitizer saturation. Vertical dotted lines mark the acquisition interval.

cyclotron and electron plasma frequencies was extended to $\omega_{ce}/\omega_{pe} > 3$, in the ballpark of ITER start-up values. Electromagnetic fluctuations generated by coupling with plasma waves were detected by means of different diagnostic settings, employing a log-periodic antenna, an adjustable dipole antenna, a low noise amplifier, a spectrum analyzer and a PXIe-5186 fast digitizer. The maximum used sampling rate was 6.25 GHz, corresponding to 0.1 s recording duration. Radio emissions were detected in all examined discharges with significant RE signatures, HXR emission in particular. Both bursting and continuous emissions have been found. An example of detected bursting emission is shown in figure 3. Radio bursts appear already in the current ramp-up phase, showing that kinetic instabilities influence RE dynamics already in the formation phase. Radio bursts are accompanied in most cases by rapid enhancements of ECE and by bursts of the Cherenkov probe signal. Suprathermal ECE is sensitive to RE perpendicular momentum, while Cherenkov probes detect escaping electrons at an equatorial location in the limiter shadow. Both observations are consistent with the occurrence of the so called anomalous Doppler (or fan) instability, which gives rise to rapid pitch-angle scattering of REs. The anomalous Doppler instability is driven by anisotropy of the momentum distribution function, a naturally occurring condition for RE electrons. Unstable waves with frequency falling in the observed spectral range (0.4–3.0 GHz)

can be either whistlers or magnetized plasma waves. The latter are favored at the high ω_{ce}/ω_{pe} values explored in FTU, for which whistlers can only resonate with RE at high-energies (> 15 MeV typical); however, further studies and multimachine comparisons are required to assess the relative importance of involved wave branches.

5. Tearing modes stabilization by electron cyclotron heating

The study of the tearing mode (TM) stability [15, 16] is an important issue for tokamak fusion devices, because the development of the magnetic islands characterizing the instability can deteriorate the confinement, leading to a decrease of the plasma energy content and sometimes to a plasma disruption. In sawtooth-free low-density regimes, magnetic islands formed by tearing instabilities around the $q = 2$ surface can appear and saturate at large amplitudes. This behaviour is common to most tokamak fusion devices, so it is important to improve the possible stabilization strategies. To this purpose, TM stabilization by ECH has been performed in sawtooth-free scenarios at low density. The ECH deposition has been varied in real time around the $q = 2$ surface, with a 'sweeping' strategy similar to the one tested in AUG [17], allowing us to relax the accuracy on the estimates of the island O-point position [18]. The present strategy might be inserted in a simple 'search and suppress' real-time control system not provided of island localization [19].

In figure 4, pulse 43055 is reported to show the free TM evolution (without injection of EC power): TM rotates and grows while its width is below a critical value; after crossing it, the TM will lock to the wall rotating at few tenths of Hz. In pulse 43154, the ECH launcher antenna is piloted with a predefined sinusoidal trajectory to only partly cover the island from the outside. The deposition radius of the beam centre (having a waist of around 2 cm, while the island is 4 cm wide) is shown together with the expected position of the $q = 2$ surface (yellow), as estimated in previous pulses carried out at fixed antenna position (with a resolution of ~ 1 cm) by varying the magnetic field (5.0, 5.3, 5.6 T). The gyrotron is triggered in real time by the amplitude of the saddle signal. When the beam centre is located at about 1.0–2.0 cm from the O-point, the effects on the TM are negligible. Mode amplitude is growing and frequency changing like in the reference pulse. ECH deposition is moved closer to the O-point, and stabilising effects are seen when deposition is close to the expected $q = 2$ position: both amplitude and mode frequency are partly recovered. Afterwards, ECH deposition is moved away, leaving the TM to continue its free evolution, which leads to large amplitude and slow rotations after the gyrotron is switched off. In pulse 43153, the launcher antenna is steered to cover the foreseen island O-point location, and slightly inward from the $q = 2$ surface. When the mode amplitude overcomes the set threshold, and gyrotron is triggered, the antenna is aiming at the O-point and then ECH power provides very fast stabilisation of the mode in 20 ms, that is 60% less than in pulses with fixed antenna. The technique was applied in a later phase on quasi-locked modes with a deposition 1.3–2.6 cm inside the
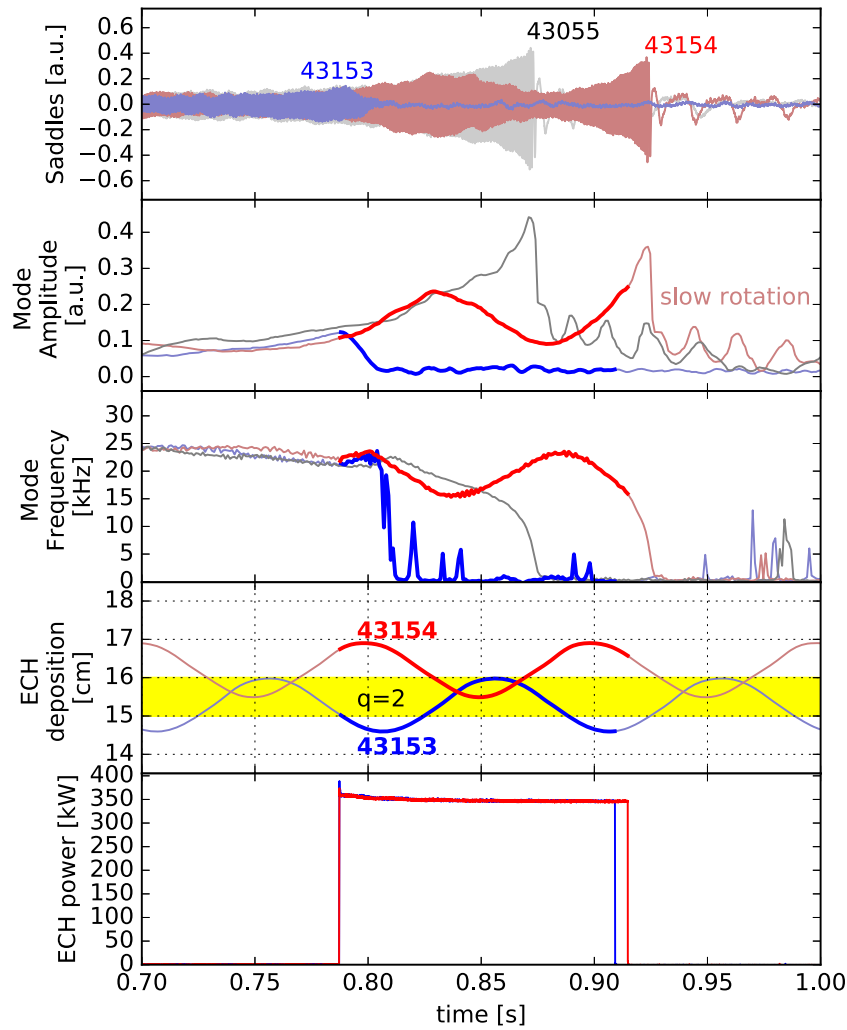
Figure 4. Tearing modes stabilization by electron cyclotron heating. From top to bottom: saddle coils raw signals, mode amplitude and frequency estimates from saddle coils signals, ECH deposition minor radius, gyrotron power. Pulse 43055 (gray) is taken as reference (no ECH injected); in 43154 (red) ECH is injected in the outer proximity of the magnetic island; in pulse 43153 (blue) ECH antenna aims at the island O-point when gyrotron power is switched on.

$q = 2$. ECH power was deposited still inside it and showed a partial reduction of the amplitude and an increase in the island rotation frequency.

6. Tearing modes stabilization by pellet injection

In order to provide alternative or parallel TM stabilization strategies, the effect of D_2 pellet injection on the temporal evolution of the magnetic island characterizing the sawtooth-free low-density regimes on FTU has been studied. A single pellet, containing around $1 \times 10^{20} D_2$ atoms, has been injected at about 1.2 km s^{-1} from the low field side mid-plane, with most of particles deposited in the core plasma. A mode stabilization in a few milliseconds has been observed after a pellet injection in presence of a fast rotating magnetic island (figure 5, left). Instead, a pellet injection in the presence of a quasi-locked magnetic island has induced a reduction of the mode amplitude and an increase of the rotation frequency (figure 5, right), preventing a dangerous complete locking. Tearing stability analysis are planned to get some insight in the stabilization process,

in particular to understand if the observed complete or partial mode stabilization could be explained in terms of the evolution of the current density profile in a relatively short resistive diffusion time scale or if it is necessary to consider local effects due to the pellet ablation [20].

7. MHD limit cycles

A peculiar MHD activity was discovered in the past on FTU, with an $m/n = 2/1$ TM (m and n are the poloidal and toroidal mode number, respectively) characterized by amplitude and frequency oscillations giving rise to 'limit cycles' in the island amplitude/frequency plane [21]. New observations have been performed, starting with sawtooth-free low-density pulses characterized by a one-to-one relation between amplitude and frequency. In these pulses, a transition to limit cycles behaviour has been obtained by neon injection, with the corresponding appearance of sawtooth activity, suggesting an interaction between the two kind of instability. An example of such behavior is reported in figure 6 (neon injected from 0.72 s to
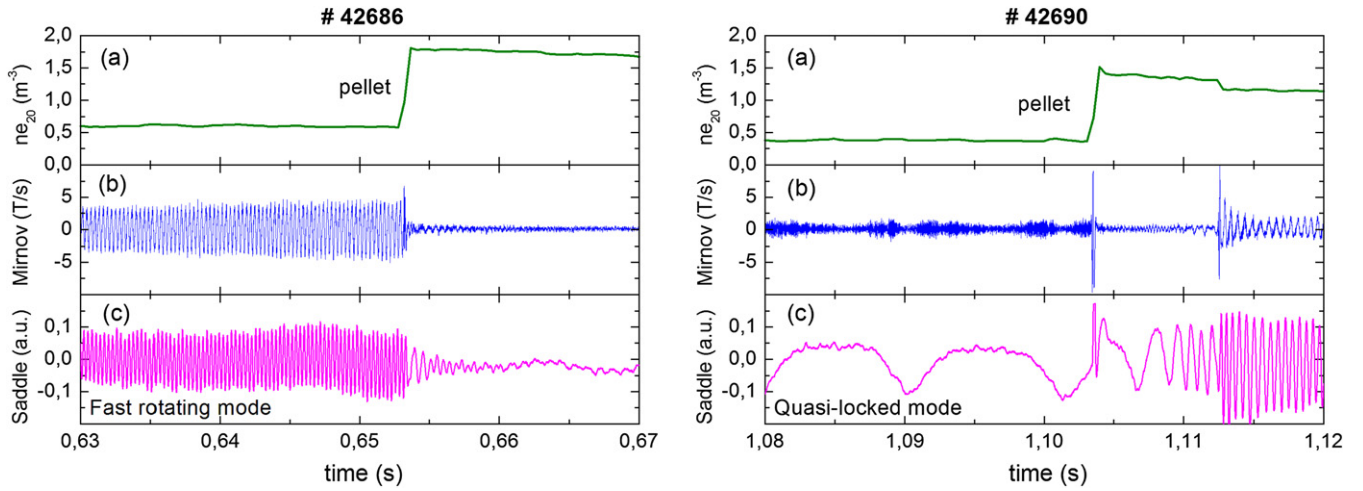
Figure 5. Tearing modes stabilization by pellet injection. FTU pulses ($B_T = 6$ T, $I_p = 0.50$ MA) with a fast rotating mode (left) and with a quasi-locked mode (right), respectively. From top to bottom: (*a*) line-averaged density for a central chord, (*b*) derivative of the poloidal magnetic perturbation from a Mirnov coil, (*c*) derivative of the radial magnetic perturbation from a saddle coil. The pellet injection corresponds to the rapid increase in density.
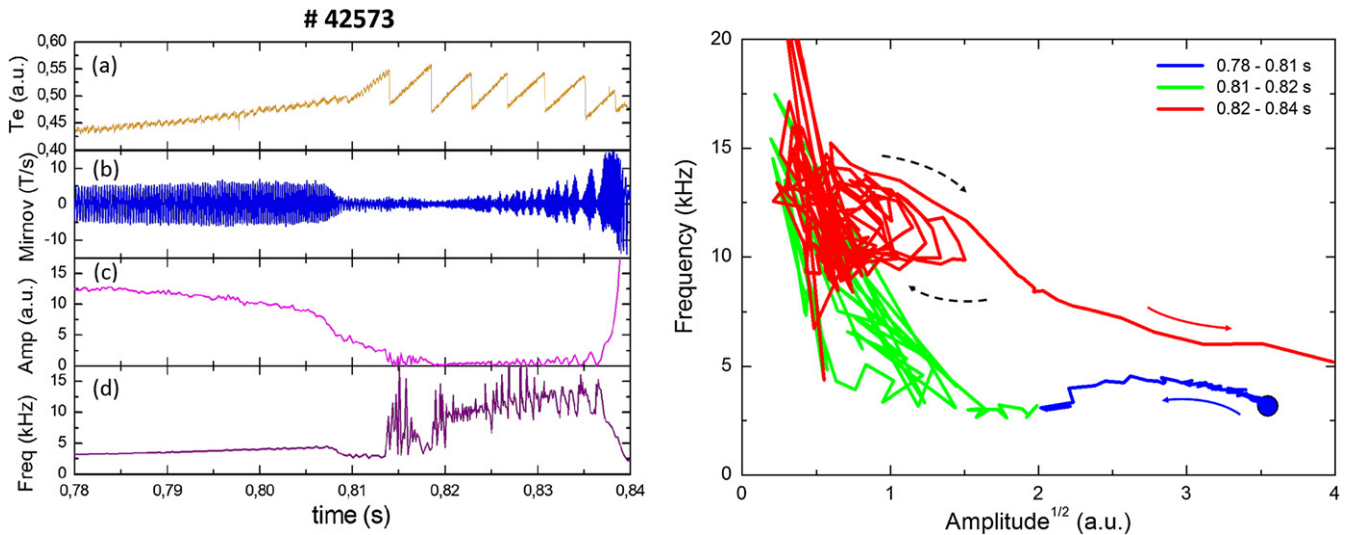

Figure 6. MHD limit cycles. FTU pulse 42573 ($B_T = 6$ T, $I_p = 0.50$ MA). (Left) From top to bottom: (*a*) central electron temperature, (*b*) derivative of the poloidal magnetic perturbation from a Mirnov coil, (*c*) mode amplitude, (*d*) mode frequency. (Right) Temporal evolution of the TM (see the legend for the meaning of the colors).

0.75 s). It is important to note that cyclic behaviors appear at mode amplitudes much smaller than pre-injection ones (the amplitude square root is considered in figure 6, right, being roughly proportional to the island width).

8. Behaviour of heavy metal ions

The high-resolution spectrometer SOXMOS [22] and the survey spectrometer SPRED [23] have allowed the identification of new, or better resolved, spectral features of tin originating from the tin liquid limiter (TLL), tungsten, and yttrium (injected by the LBO technique). Besides a few well isolated lines, the spectra emitted by heavy elements are characterized by unresolved transition arrays; the aim of the experiments was to identify them to use for prompt monitoring of the plasma

level of contamination, especially in the presence of other intrinsic metal impurities such as molybdenum or stainless steel components. All of the discharges had a plasma density of about 0.6×10^{20} m^{-3} and electron temperatures ranging from 1.2 to 2 keV.

The lines of tin (figure 7(*a*)) were identified as emission from Sn IX to XXII ionization states, localized between $r/a = 0.75$ and 0.85 of the plasma column. In a series of repetitive discharges all ending in disruption, the Sn seems to gradually replace the Mo emission, yet remaining at similar levels of contamination. Tungsten (figure 7(*b*)) is a material of interest for plasma facing components (PFCs), but experimental data for such a heavy element are not yet exhaustive and the atomic data are difficult to calculate. The recorded spectral features from W XXVIII to XXX confirm previous observations; the
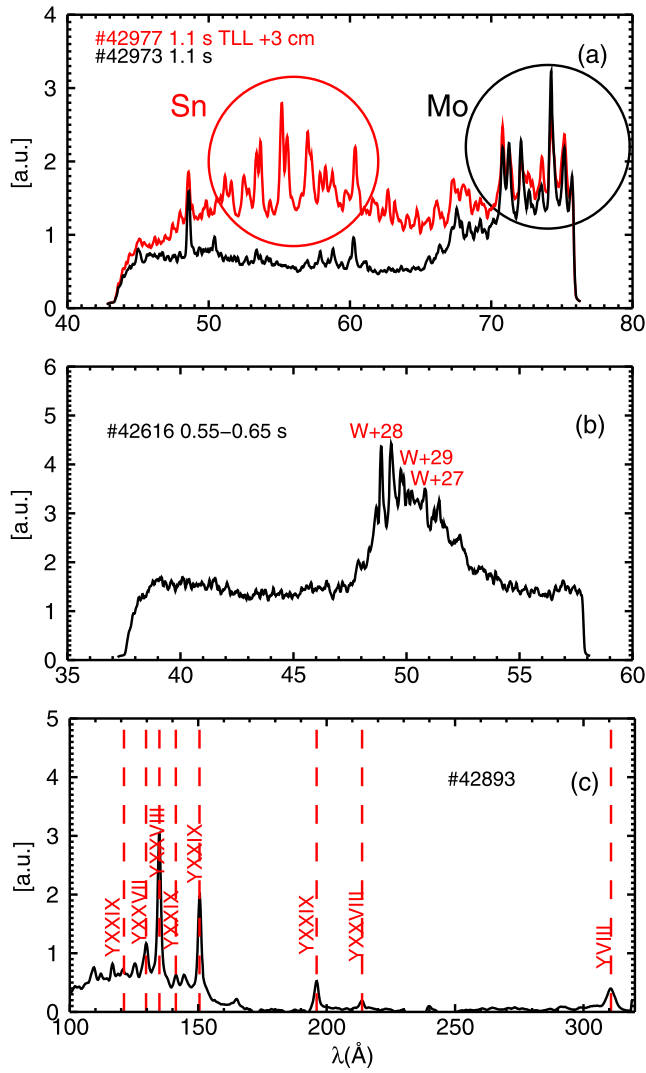
Figure 7. Behaviour of heavy metal ions. From top to bottom: (*a*) spectrum of Sn, compared to the standard Mo-dominated one, measured by the SOXMOS spectrometer in plasma discharges with ECRH, $B_T = 5$ T, $I_p = 0.5$ MA, and the TLL inserted 3 cm into the vacuum vessel (in red) or fully retracted (in black); (*b*) spectrum of W measured by the SOXMOS spectrometer following LBO injection at $B_T = 5$ T, $I_p = 0.75$ MA; (*c*) spectrum of Y measured by the SPRED spectrometer following LBO injection at 0.5 s, resulting from the difference between the spectrum taken 60 ms after the LBO injection and the one just before it ($B_T = 5$ T, $I_p = 0.35$ MA).

associated coronal equilibrium calculations localize those ion stages at the core/medium radius regions of FTU. The analysis of the time behaviours of experimental radiated power emissivity profiles and soft x-rays central brightness indicate that W reaches the plasma center but does not accumulate, as expected in these L-mode plasmas. Few lines of yttrium were clearly visible in the 100–300 Å spectral range and could be properly identified, whereas no distinct lines emerged at lower wavelength. The spectrum shown in figure 7(*c*) is the difference between the spectrum measured 60 ms after the injection, at the time when the Y emission is at its peak, and the one taken just before it.

9. Helium doped plasmas

The light doping action represents a good method to increase the core electron density, often without any undesirable central impurity accumulation [24]; meanwhile, the amount of impurities and the relative edge radiation have to be kept below the threshold where a disruptive MHD activity is generated. This scenario favors the so-called 'plasma detachment'. In order to extend experimental observations regarding the electron density peaking in doped plasma [25], a series of experimental sessions have been performed in the last two campaigns by injecting helium on the L-mode plasma scenarios. The valve utilized for helium injection can be settled by acting both on final valve pressure drop ΔP (expressed in mbar), proportional to the total amount of helium injected (the valve pre-chamber has a volume of 37 cm^3), and on the valve voltage, which controls the rate of injection: the higher the voltage, the faster the injection. As first results, it has been revealed that not only the total amount of helium injected, but also the rate of injection, as well as edge conditioning, can influence the impurity effects. Examples are exposed in figure 8.

VUV spectroscopy measurements help to evaluate the helium presence, which triggers the particles inflow. To establish the quantity of the impurities species in these plasmas, an approximated model has been developed, based upon a multi unknowns system that uses measurements of Z effective charge, as well as the radiation losses and the VUV spectroscopy. A good assessment in the estimation of the species concentrations was found. Considerable effort has been devoted to the search of the best conditions to obtain a very high electron density peaking, defined as the ratio $n_{e0}/\langle n_e \rangle_{vol}$ between the central density and the volume-averaged density. In particular, a scan of plasma current ($I_p = 250$–500 kA, $B_T = 5.3$ T, $n_{e0} = 0.2$–1.0×10^{20} m^{-3}, $T_{e0} = 1$–4 keV) has confirmed that the highest peaking is obtained at low current, by reaching the value of 5, which is a very high value in the world tokamak scene. Furthermore, different scenarios have been experimentally performed, exploring the relationship between the increase of the electron density and the plasma position inside of the wall chamber, by varying plasma shape and magnetic configuration.

10. Electron cyclotron assisted start-up

As in superconducting future tokamaks (JT-60SA, ITER and DEMO) the plasma start-up will be uniquely assisted with EC power, the experimental study and simulation of the conditions for reliable plasma start-up are clearly of great interest [26]. Start-up assisted with EC (both X2 and O1 polarizations) experiments have been performed at reduced electric field (about 0.5 V m^{-1}) in the presence of different Ne impurity content to mimic the conditions for a new pulse after a disruption. The EC resonance was moved off-axis (by varying the toroidal magnetic field) at a fixed poloidal magnetic configuration to explore the influence of the relative position of EC absorption layer and poloidal field-null region [27]. In the
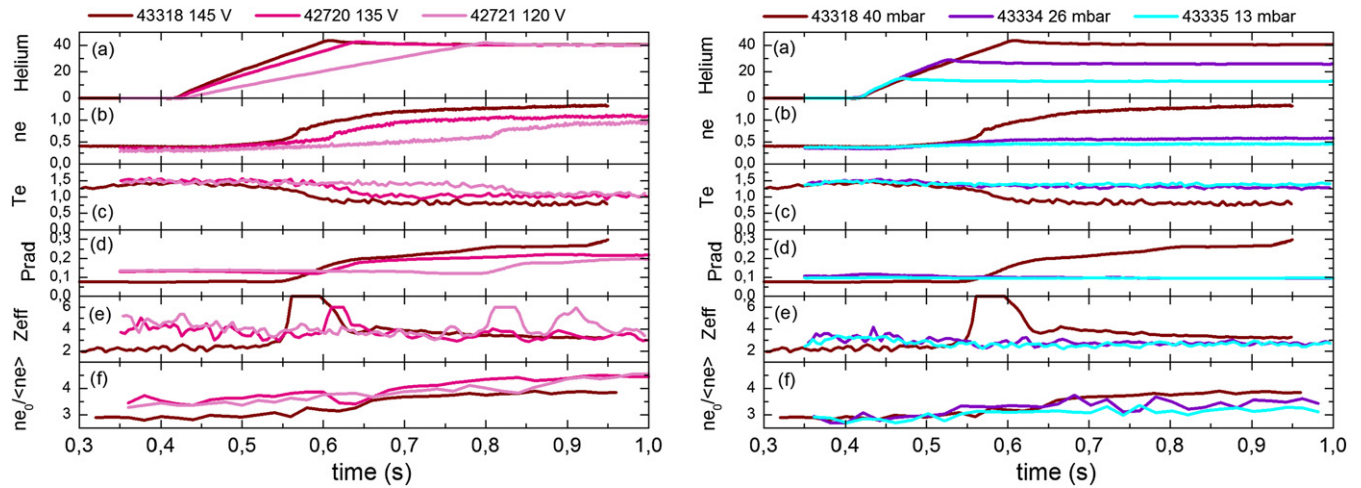
Figure 8. Helium doped plasmas. (Left) Valve voltage scan ($\Delta V = 120-145$ V) for a fixed amount of total helium injected ($\Delta P = 40$ mbar). (Right) Helium scan ($\Delta P = 13-40$ mbar) for a fixed valve voltage ($\Delta V = 145$ V). (*a*) Temporal evolution of cumulative helium injection, depending on the valve voltage and on the total pre-programmed amount. (*b*) Electron density in 10^{20} m^{-3}, with a faster and higher increase when the valve is at maximum voltage (left) and with weak modifications at minimum injected impurity (right). (*c*) Electron temperature in keV, showing that, during the injection phase, the plasma is colder when the rate of the gas puff is greater. (*d*) Radiation losses in MW, following the electron density trend. (*e*) Effective charge signals, highlighting that, unfortunately, all of these plasmas contain other impurities besides helium. (*f*) Density peaking, starting to rise about 100 ms after the helium puff (at 0.4 s).
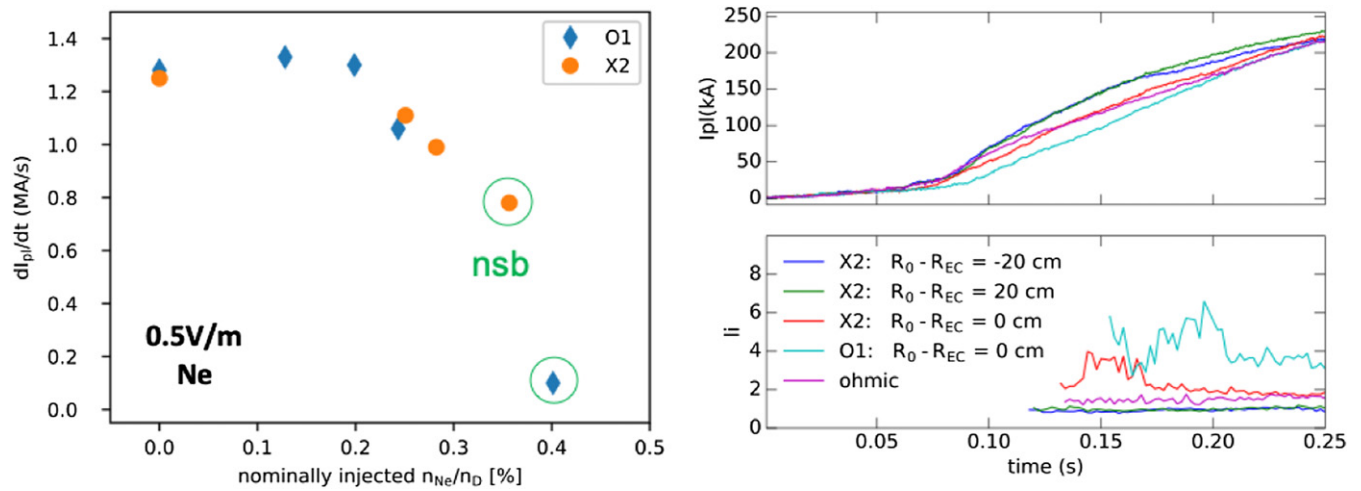

Figure 9. Electron cyclotron assisted start-up. (Left) Current rise as a function of impurity content in EC assisted experiment. Points in green circles represent the conditions where the start-up is not sustained. The effectiveness of EC does not depend on polarization. (Right) Time traces of plasma current and internal inductance for off-axis and on-axis EC resonances. Here O1 refers to ordinary mode in case of fundamental resonance and X2 to extraordinary mode for the second harmonic; R_0 is the major radius of the magnetic axis while R_{EC} refers to the EC resonance.

first case (figure 9, left), the impurity influences plasma resistivity making the ECRH necessary to pass the burn-through. In the second case (figure 9, right), the off-axis case leads to a reduction of the internal inductance suggesting a wider current profile supported by a faster current ramp-up. In the on-axis case, the current shrinking is confirmed by higher internal inductance and by a stronger MHD activity.

11. High temperature plasmas

Electron temperature up to 14 keV was obtained in EC heated pulses on current ramp-up. A systematic disagreement

between the Thomson scattering and ECE measurements was found. This could be explained in terms of distortion of the electron distribution function [28]. In figure 10(*a*), the time behaviour of the electron temperature measured by Thomson scattering (Te_{TS}, blue symbols) and the one measured by ECE (Te_{ECE}, red line) is shown for the pulse 43100, where the maximum temperature of 14 keV is measured. It turns out that for temperature below 8 keV the two measurements agree inside the error bar, while for $Te_{TS} > 8$ keV the two measurements are different. The measurement of Te_{TS} corresponds to the position of the scattering volume in the $z = 2$ cm over the equatorial plane [29], while the measurement of Te_{ECE} corresponds to the
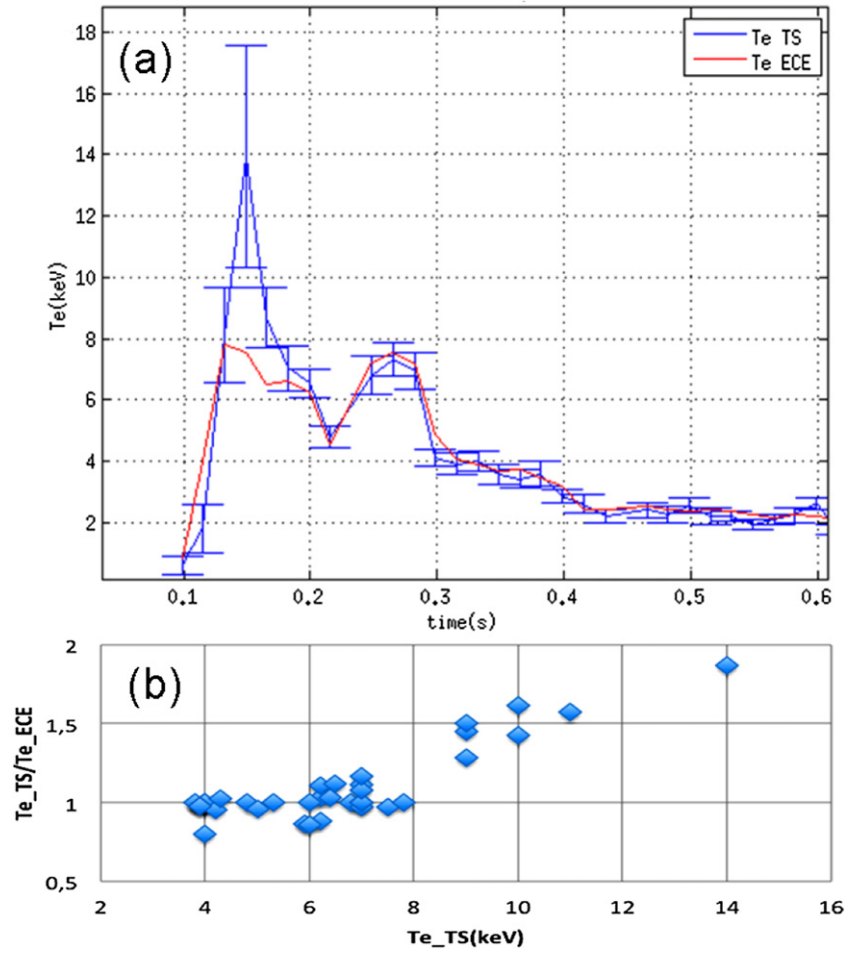
Figure 10. High temperature plasmas. (*a*) Electron temperature, in keV, versus time for FTU pulse 43100. Te_{TS} in blue, Te_{ECE} in red. (*b*) Ratio Te_{TS}/Te_{ECE} versus Te_{TS} for FTU pulses 43099, 43100, 43101.
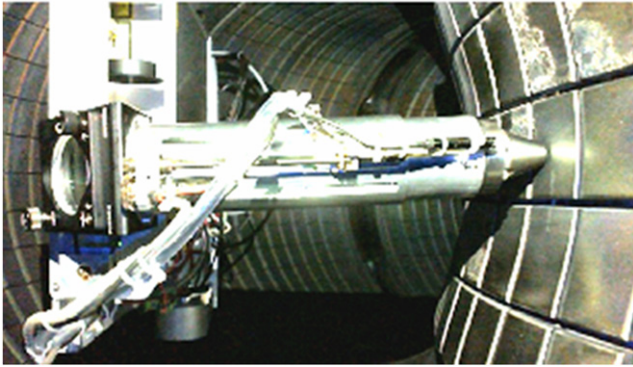

Figure 11. Laser induced breakdown spectroscopy. The LIBS device measuring inside the FTU vacuum vessel on a tile of the toroidal limiter.

maximum electron temperature measured by Michelson interferometer looking into a line of sight along the equatorial plane [30] with a space resolution of 3 cm. The data related to the pulses 43099, 43100 and 43101 are collected in the plot shown in figure 10(*b*), where the ratio Te_{TS}/Te_{ECE} is reported versus Te_{TS}.

12. Diagnostics

12.1. Laser induced breakdown spectroscopy

Currently, the laser induced breakdown spectroscopy (LIBS) is one of the most eligible techniques for the *in situ* chemical characterization of PFCs also under consideration for the detection of tritium retained in the ITER vacuum vessel. LIBS is a rapid chemical analysis technology in which a short laser pulse is focused onto the sample surface to create a micro-plasma. The plasma light is collected and focused on the optical fiber and finally dispersed on one or more spectrographs, providing information on the atomic composition of the target. As a proof-of-concept, the chemical analysis of the FTU first wall and toroidal limiter was performed after the FTU spring-summer 2019 experimental campaign. For this purpose, a new LIBS system was recently designed, developed and mounted on the FTU robotic arm, entering inside the FTU vessel and acquiring two simultaneous LIBS spectra with a bifurcated optical fiber. The first in a wide spectral region (210–800 nm), to detect as much as possible emission lines from all of the chemical elements; the second in a restricted spectral region (8–20 nm), with very high
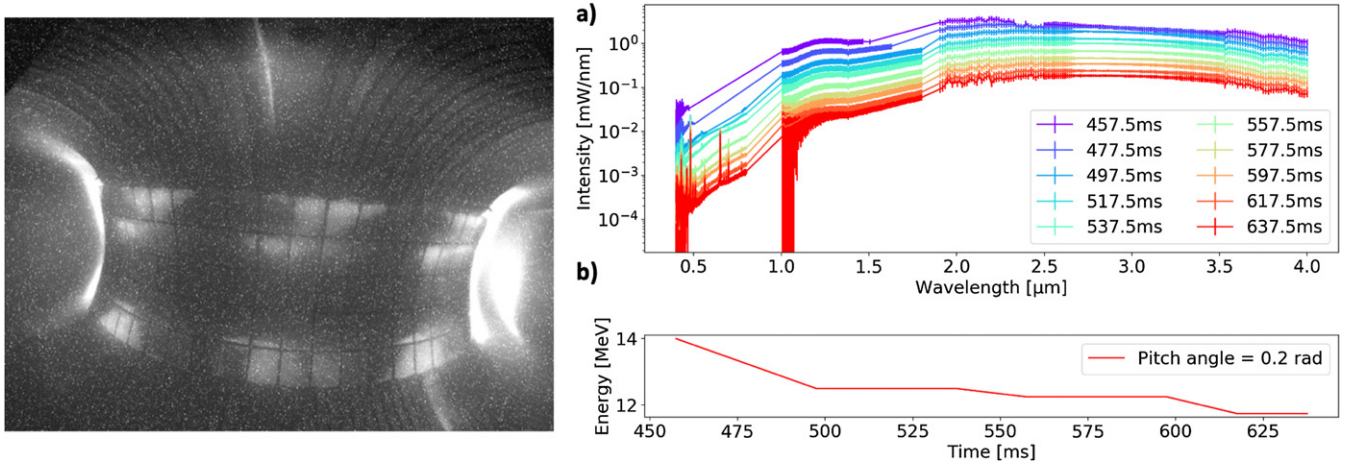
Figure 12. Runaway electron imaging spectrometry system. RE in shot 43654. (Left) Visible camera image from REIS-E (*t* = 360 ms, pre-disruption phase). (Right) (*a*) Calibrated RE signal interpolated from the three forward view spectrometers (post-disruption phase); (*b*) RE energy reconstruction by means of SOFT analysis based on camera and spectrometers data.
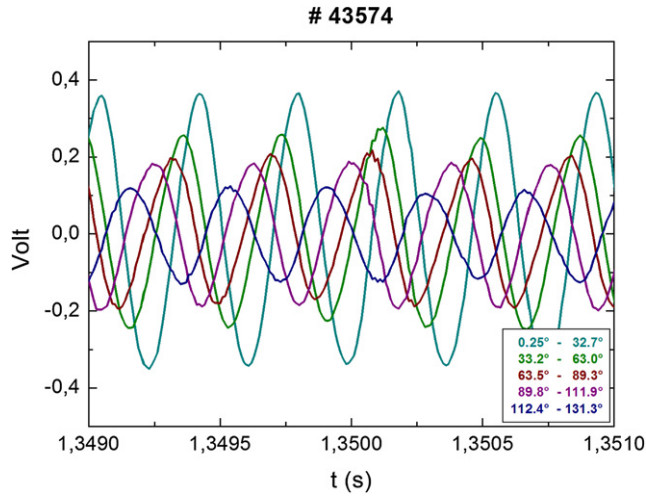

Figure 13. High resolution saddle coil array. Time evolution of signals coming from five saddle coils of the same toroidal sector at five different poloidal locations (see the legend for the minimum/maximum poloidal angles) in presence of a 2/1 rotating magnetic island. The phase-differences are related to the poloidal mode number, whilst the signal amplitudes are approximately proportional to the area of each coil.
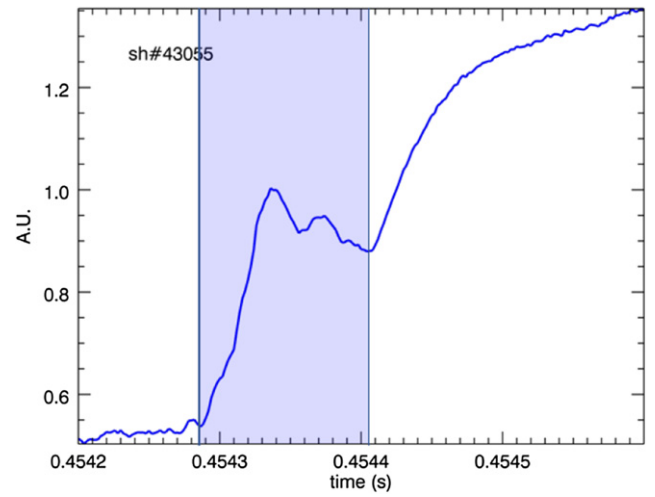

Figure 14. Diamond detectors for fast VUV and SXR diagnostics. Time evolution of the ablation process (shaded area) of a pellet injected into an FTU plasma from the low field side, as recorded by the diamond detector.

resolution, to resolve very close emission lines. To our knowledge, this is the first prototype of such a device mounted on a robotic arm [31]. Its main features are: (1) compactness (about $410 \times 300 \times 70$ mm), weight (10 kg); (2) the possibility of acquiring two simultaneous LIBS spectra; (3) to perform measurements in vacuum (down to 10^{-3} mbar) or under gas flow (e.g. Ar, He, N2, etc); (4) to operate also in double pulse mode for an increased sensitivity. The analysis of the FTU PFCs revealed their main chemical components including Mo, Ti from the TZM tiles of the toroidal limiter, the stainless steel components of the first wall, and an overall superficial contamination of Li, due to the above mentioned liquid lithium limiter experiments. A quantification of the different elements cannot be provided at the moment, as it requires the completion of the calibration procedure of the lines of all of the elements

present. In figure 11, a picture of the system measuring inside the FTU vessel is shown.

12.2. Runaway electron imaging spectrometry system

An upgrade of the REIS [32] system has been carried out recently. The range of the measured synchrotron radiation spectra emitted by REs is now from 0.4 up to 5 μm. The REIS-E (extended) spectrometry system is currently composed of four different spectrometers: visible (VIS), near infrared (NIR), mid-infrared (MIR) spectrometers for the tokamak forward view and a VIS spectrometer for the backward view. These are connected to the diagnostic head by a multimode InF$_3$-ZrF$_4$-low OH trifurcated fiber bundle (19 m). The images are collected with a fast CCD camera with 111° FOV. Both systems collect the light through a custom optics made of CaF$_2$ lenses. The system was tested during the FTU 2019

experimental campaign. The camera and the new spectrometer were integrated into the acquisition software, based on LabVIEW. The spectrometers were calibrated with a tungsten halogen source and an IR tungsten source up to 5 μm, after the data campaign. The integration acquisition time was set at 15 ms for all spectrometers. The diagnostic acquired data in the FTU RE experiments collect several RE beam signals. The analysis is ongoing and it based on the comparison of experimental images and spectra with those simulated using SOFT [33]: the RE energy, pitch angle and radial profile have been inferred. An example of the experimental and simulated data is shown in figure 12.

12.3. High resolution saddle coil array

A set of 16 saddle coils covering all of the poloidal contours is present at four different toroidal positions in FTU. The saddle coils are displaced following magnetic coordinates [34] and the change of magnetic flux through each saddle is usually acquired at 2 kHz and integrated.

Recently, the signals coming from eight saddles covering the $z > 0$ region of a toroidal sector and from the equatorial saddle in the low field side of the other three toroidal sectors have been acquired at 250 kHz, without temporal integration, allowing the observation of the radial magnetic perturbation associated to MHD activities also at lower frequencies (thanks to their large area), where the Mirnov coils are limited by the external transformer acting as high-pass filter. These observations showed the capability of this high resolution saddle coil array to evaluate the toroidal and poloidal mode number of TMs in a large range of frequencies above the inverse of the FTU wall time. The time evolution of signals from different saddle coils in the presence of a 2/1 TM is reported in figure 13.

12.4. Diamond detectors for fast VUV and SXR diagnostics

Two photodetectors based on synthetic single crystal diamonds and optimized, respectively, for extreme UV and SX detection, were installed on FTU and tested on different plasma scenarios during the latest experimental campaign. They were developed at Tor Vergata University of Rome, using a p-type/intrinsic/Schottky metal contact configuration, which allows operation at or above room temperature with no external applied voltage and high sampling rates (500 kHz) [35]. Plasma fast events, such as the pellet ablation process shown in figure 14, can be followed in great detail with high S/N ratio, and compared with other diagnostics. These preliminary measurements have opened up the possibility of a much wider range of application for this type of detectors, for example its use as complementary fast bolometer in the range 10–10 000 eV. A dedicated R & D activity was started, aimed at the design of a prototype diamond tomography/bolometer system covering an extended energy range.

13. Conclusions

Since the 2018 IAEA FEC Conference, FTU operations have been devoted to several programs covering a large range of topics. A liquid tin limiter has been used for the first time in a tokamak and several experiments have shown that if the liquid tin surface temperature is below the evaporation onset (namely below 1500 °C) the plasma performances appear unaffected, with heat loads up to 18 MW m^{-2}. Experiments on multiple D_2 pellet injections on quiescent REs have demonstrated the possibility to induce complete RE loss, restoring a 'safe' steady-state discharge. The emission of radio waves has been detected in pulses with significant RE signatures. Concerning the MHD studies, the complete stabilization of TMs in sawtooth-free low-density pulses has been obtained both by electron cyclotron heating (with 'sweeping' strategy) and by pellet injection (for the first time ever), and the transition from smooth to limit cycles behavior has been induced.

Other experiments have involved the high resolution spectroscopy of heavy metal ions, with the identification of lines of Sn in the peripheral region, of W at the core/medium radius regions, and of some lines of Y at higher wavelengths. The properties of He doped plasmas (e.g. the electron density peaking) have been studied by varying both the total amount of injected impurity and rate of injections. Experiments on EC assisted start-up have been performed at reduced electric field in the presence of Ne impurity, to mimic the post disruption condition in superconducting future tokamaks, showing the capability to sustain the start-up up to Ne concentration of the order of 0.4% and reduction of the internal inductance has been observed by moving the EC resonance off-axis. In addition, a systematic disagreement between the Thomson scattering and ECE temperature measurements was found at high temperatures in EC heated pulses on current ramp-up, which could be explained in terms of distortion of the electron distribution function.

The effectiveness of a new LIBS system mounted on the FTU robotic arm has been demonstrated, with the simultaneous acquisition of two different spectra. An upgrade of the REIS system for in-flight runaways studies has been carried out, with the preliminary reconstructions of the RE energy evolution by means of analysis based on camera and spectrometers data. Finally, a high resolution saddle coil array has been utilized for mode number analysis in the presence of rotating magnetic islands and UV and SXR detectors, based on synthetic single crystal diamonds, have been successfully installed and tested on different plasma scenarios.

Acknowledgments

References

[1] Gormezano C., De Marco F., Mazzitelli G., Pizzuto A., Righetti G. B. and Romanelli F. 2004 Chapter 1: The FTU Program *Fusion Sci. Technol.* **45** 297

[2] Mazzitelli G. *et al* 2017 Comparison between liquid lithium and liquid tin limiters in FTU *Proc. 44th EPS Conf. On Plasma Physics* (Belfast, Northern Ireland, UK, 26–30 June 2017) Vol. 41F O5.132 (http://ocs.ciemat.es/EPS2017PAP/pdf/O5.132.pdf)

[3] Vertkov A., Luyblinski I., Evtikhin V., Mazzitelli G., Apicella M. L., Lazarev V., Alekseyev A. and Khomyakov S. 2007 Technological aspects of liquid lithium limiter experiment on FTU tokamak *Fusion Eng. Des.* **82** 1627

[4] Vertkov A., Lyublinski I., Zharkov M., Mazzitelli G., Apicella M. L. and Iafrati M. 2017 Liquid tin limiter for FTU tokamak *Fusion Eng. Des.* **117** 130

[5] Coenen J.W. *et al* 2014 Liquid metals as alternative solution for the power exhaust of future fusion devices: status and perspective *Phys. Scr.* **2014** T159014037

[6] Mazzitelli G. *et al* 2019 Experiments on the Frascati Tokamak Upgrade with a liquid tin limiter *Nucl. Fusion* **59** 096004

[7] Roccella S., Dose G., de Luca R., Iafrati M., Mancini A. and Mazzitelli G. 2020 CPS Based Liquid Metal Divertor Target for EU-DEMO *J. Fusion Energy* **39** 462

[8] Lehnen M. *et al* 2015 Disruptions in ITER and strategies for their control and mitigation *J. Nucl. Mater.* **463** 39

[9] Carnevale D. *et al* 2019 Runaway electron beam control *Plasma Phys. Control. Fusion* **61** 014036

[10] Gobbin M. *et al* 2018 Runaway electron mitigation by 3D fields in the ASDEX-Upgrade experiment *Plasma Phys. Control. Fusion* **60** 014036

[11] Paz-Soldan C., Eidietis N.W., Liu Y.Q., Shiraki D., Boozer A.H., Hollmann E.M., Kim C.C. and Lvovskiy A. 2019 Kink instabilities of the post-disruption runaway electron beam at low safety factor *Plasma Phys. Control. Fusion* **61** 054001

[12] Boozer A.H. *et al* 2016 Runaway electrons and magnetic island confinement *Phys. Plasmas* **23** 082514

[13] Aleynikov P. and Breizman B. 2015 Stability analysis of runaway-driven waves in a tokamak *Nucl. Fusion* **55** 043014

[14] Heidbrink W.W. *et al* 2019 Low-frequency whistler waves in quiescent runaway electron plasmas *Plasma Phys. Control. Fusion* **61** 014007

[15] Furth H.P., Killeen J. and Rosenbluth M.N. 1963 Finite-Resistivity Instabilities of a Sheet Pinch *Phys. Fluids* **6** 459

[16] Furth H.P., Rutherford P.H. and Selberg H. 1973 Tearing mode in the cylindrical tokamak *Phys. Fluids* **16** 1054

[17] Maraschek M. *et al* 2015 Real-time control of MHD instabilities using ECCD in ASDEX Upgrade *Proc. 42nd EPS Conf. On Plasma Physics* (Lisbon, Portugal, 22–26 June 2015) Vol. 39E P1.112 (http://ocs.ciemat.es/EPS2015PAP/pdf/P1.112.pdf)

[18] Février O., Maget P., Lütjens H. and Beyer P. 2017 Comparison of magnetic island stabilization strategies from magnetohydrodynamic simulations *Plasma Phys. Control. Fusion* **59** 044002

[19] Felici F., Goodman T.P., Sauter O., Canal G., Coda S., Duval B.P. and Rossel J.X. 2012 Integrated real-time control of MHD instabilities using multi-beam ECRH/ECCD systems on TCV *Nucl. Fusion* **52** 074001

[20] Bardóczi L. *et al* 2019 Controlled neoclassical tearing mode (NTM) healing by fueling pellets and its impact on electron cyclotron current drive requirements for complete NTM stabilization *Nucl. Fusion* **59** 126047

[21] Pucella G., Giovannozzi E., Buratti P. and Cianfarani C. 2017 MHD limit cycles on FTU *Nucl. Fusion* **57** 116037

[22] Schwob J.L., Wouters A.W., Suckewer S. and Finkenthal M. 1987 High-resolution duo-multichannel soft x-ray spectrometer for tokamak plasma diagnostics *Rev. Sci. Instrum.* **58** 1601

[23] Fonck R.J. 1982 Multichannel grazing-incidence spectrometer for plasma impurity diagnosis: SPRED *Appl. Opt.* **21** 2115

[24] Messiaen A. *et al* 1996 High Confinement and High Density with Stationary Plasma Energy and Strong Edge Radiation in the TEXTOR-94 Tokamak *Phys. Rev. Lett.* **77** 2487

[25] Mazzotta C. *et al* 2015 Peaked density profiles due to neon injection on FTU *Nucl. Fusion* **55** 073027

[26] Granucci G. *et al* 2015 Experiments and modeling on FTU tokamak for EC assisted plasma start-up studies in ITER-like configuration *Nucl. Fusion* **55** 093025

[27] Ricci D. *et al* 2019 EC assisted start-up experiment and predictions for the next generation fusion experiments *Proc. 46th EPS Conf. On Plasma Physics* (Milan, Italy, 8–12 July) Vol. 43C O5.103 (http://ocs.ciemat.es/EPS2019PAP/pdf/O5.103.pdf)

[28] Krivenski V. 2001 Electron cyclotron emission by non-Maxwellian bulk distribution functions *Fusion Eng. Des.* **53** 23

[29] Orsitto F., Brusadin A., Giovannozzi E., Santi D., Bartiromo R. and Pizzolati P. 1995 Thomson scattering system on FTU tokamak: Calibration, operation, results *Rev. Sci. Instrum.* **66** 1167

[30] Buratti P., Tudisco O. and Zerbini M. 1993 A broadband light collection system for ECE diagnostics on the FTU tokamak *Infrared Phys.* **34** 533

[31] Almaviva S. *et al* 2020 LIBS measurements inside the FTU vessel mock-up by using a robotic arm *Fusion Eng. Des.* **157** 111685

[32] Causa F. *et al* 2019 Runaway electron imaging spectrometry (REIS) system *Rev. Sci. Instrum.* **90** 073501

[33] Hoppe M., Embréus O., Tinguely R.A., Granetz R.S., Stahl A. and Fülöp T. 2018 SOFT: a synthetic synchrotron diagnostic for runaway electrons *Nucl. Fusion* **58** 026032

[34] Alladio F. and Crisanti F. 1986 Analysis of MHD equilibria by toroidal multipolar expansions *Nucl. Fusion* **26** 1143

[35] Cesaroni S. *et al* 2021 CVD diamond photodetectors for FTU plasma diagnostics *Fusion Eng. Des.* **166** 112323